PAPER

Check for updates

Kinetic modeling of ammonia and hydrogen dissociative co-adsorption on iron surface and its effect on hydrogen embrittlement

Nan Zhang,[*ac] Kentaro Wada,[a] Ryuoske Komoda,[b] Aleksandar Staykov [a] and Masanobu Kubota[*a]

We study the mitigation of environmental hydrogen embrittlement of iron by ammonia impurities in the hydrogen gas using combined theoretical and experimental methods. The competitive and dissociative co-adsorption of gaseous ammonia and gaseous hydrogen on the iron surface was investigated using density functional theory. The surface adsorption and decomposition of ammonia, as well as the ammonia partial pressure, were considered as influential factors contributing to the control of atomistic hydrogen uptake into the material. To elucidate the mechanism of ammonia competing with hydrogen on the iron surface and of ammonia mitigating hydrogen embrittlement, we develop kinetic modeling that can estimate the reaction rate and the dynamic surface coverage of different adsorbed species on the iron surface. The reaction rates for hydrogen and ammonia co-adsorption and dissociation were calculated using transition state theory combined with the Langmuir adsorption model, and a fracture toughness test was conducted to validate theoretical results. The adsorption rate of ammonia on iron is significantly higher compared to hydrogen, thus, ammonia hinders the hydrogen adsorption on the iron surface. However, partial pressure dependent ammonia decomposition also provides hydrogen atoms, which induce hydrogen embrittlement. The theoretical results of this study were supported well by experimental fracture toughness test results.

1. Introduction

The combination of environmental and economic factors led to the wider adoption of hydrogen as an energy source and energy storage compound. The abundance of renewable energy sources combined with steam electrolyzes could successfully convert renewable energy into chemical fuel (H_2) that can be stored and transported over long distances. Hydrogen can be utilized in the chemical industry, in fuel cells for stationary and mobile generation of electricity, and in combustion turbines on its own or in mixtures with hydrocarbons. However, hydrogen causes degradation of material strength of metal components such as storage containers and pipelines, which is generally known as hydrogen embrittlement (HE) of metals. HE is caused by the diffusion of hydrogen atoms into the metal lattice, leading to the formation of brittle hydride phases,[1] weakening

of metal bonds,[2] enhancement of localized plasticity,[3] and so on resulting in lower resistance to fracture, which can cause sudden and catastrophic failure. HE manifests as ductility loss in the tensile tests, fatigue crack growth acceleration, and fracture toughness reduction.[4–8] In the gaseous hydrogen environment, hydrogen uptake from the environment into the material is the first step for HE of iron (Fe) and steel. In the process of hydrogen uptake at room temperature, the dissociation of hydrogen molecules into hydrogen atoms is assisted by catalysis of the iron surface.[9] In this context, if the catalysis of the Fe surface is suppressed by surface catalytic poisons the HE could be significantly delayed.[10–16] The strategy of adding ppm level gaseous impurities to the hydrogen gas to mitigate the HE is attracting more attention because the impurity mitigation strategy allows us to use the existing steel pipelines and storage vessels utilized for natural gas without the construction of expensive, hydrogen resistant infrastructure. For instance, the well-established natural gas pipeline could be employed for hydrogen gas transportation. The impurity mitigation strategy has the potential to accelerate the adoption of hydrogen energy at reduced cost. Nagao *et al.* experimentally demonstrated that exposure of the SCM435 low-alloy steel, whose surface is covered by a natural oxide layer, to 120 MPa H_2 gas at room

a International Institute for Carbon Neutral Research, Kyushu University, Fukuoka, Japan

b Department of Mechanical and Control Engineering, Kyushu Institute of Technology, Kitakyushu, Japan

c Department of Mechanical Engineering, Nagaoka University of Technology, Nagaoka, Japan. E-mail: nanzhang@vos.nagaokaut.ac.jp

This journal is © the Owner Societies 2025

Phys. Chem. Chem. Phys., 2025, **27**, 24589–24600 | **24589**

temperature caused no increase in the hydrogen concentration in the material.[17] It implies that hydrogen uptake from H_2 gas into the steel at room temperature requires fresh iron surface, which can act as a catalytic site for the dissociation of molecular hydrogen into atomic hydrogen. Fresh iron surface is created by crack propagation initially through the native oxide layer.[18] Staykov et al. explained the role of the iron surface as a catalyst for the dissociation of H_2 molecules by density functional theory (DFT) calculations and elucidated the mechanism of O_2 mitigation effect on HE.[19] The iron surface should be clean in order to act as a catalyst for the H_2 dissociation. Preadsorbed oxygen on the iron surface hinders the catalytic activity by localization of the electron density. Somerday et al. considered that the hydrogen uptake from hydrogen gas occurs at the newly created surfaces during crack propagation. They experimentally confirmed both the hydrogen uptake through the surfaces created during crack propagation and the blocking of hydrogen uptake by preadsorbed oxygen based on their crack propagation tests of X52 steel.[20]

In addition to oxygen, carbon monoxide (CO) is well-studied as a mitigator of HE.[21,22] Komoda et al. clarified the mitigation effects of CO and O_2 on the HE is focusing on their adsorption rates on the iron surface. Staykov et al. theoretically calculated the ratio of the impurity-occupied sites to free sites on the surface in order to interpret the result of the fracture toughness tests.[21] They showed that O_2 coverage is 100%, while that of CO is less than 75%.[21,22] These results are useful for understanding the different HE mitigation properties of O_2 and CO impurities. While both O_2 and CO show excellent HE mitigation effects, there are some limitations to their industrial applications. For example, O_2 forms explosive mixtures with H_2 at higher concentrations, thus mixing O_2 and H_2 is considered a safety issue.[23] CO is a catalytic poison for platinum nanoparticles in polymer electrolyte fuel cell and is an undesired impurity for industrial applications.[24] CO mitigation effect is also limited to low pressure and short time intervals owing to the incomplete surface coverage. Thus, the mitigation effects of these impurities should be utilized in their respective suitable contexts. Therefore, to industrially use the mitigation effects of impurities more broadly, it is necessary to comprehensively elucidate the influences of other impurities besides O_2 and CO.

In this context, we focused on ammonia (NH_3) because it does not imply industrial safety issues and does not have a poisoning effect on the catalytic activity of platinum. However, the number of studies on the effect of NH_3 on HE is very limited. Srikrishnan et al. reported that NH_3 mitigated hydrogen-assisted crack growth of iron.[25] They carried out the crack growth experiment of 4340 steel under H_2 gas and H_2 gas mixed with 50 ppm in volume (vppm) NH_3 at 330 Pa of gas pressure, the result showed that the 50 vppm NH_3 significantly reduced the crack growth speed compared with that in the pure H_2. On the other hand, NH_3 induces stress corrosion cracking, which is one of the forms of hydrogen embrittlement.[26] Also, degradation of the tensile strength properties is induced in the NH_3 environment.[27] Thus, the effect of NH_3 on HE is

complicated as it can both mitigate and induce HE. The mitigation mechanism of NH_3 on HE remains unclear.

In addition to first-principles energetics, a kinetic framework is needed to translate elementary adsorption and dissociation steps into observable surface coverages and rates under realistic gas compositions. A mean-field (Langmuir-type) microkinetic treatment provides this bridge by mapping DFT-derived barriers and adsorption energies to competitive and dissociative co-adsorption of NH_3 and H_2, thereby rationalizing how partial pressures and temperature control the instantaneous availability of catalytic sites and the net hydrogen supply to iron. Such models are widely used as a pragmatic baseline for trend-level comparisons and for screening mitigation strategies, especially when experiments alone cannot resolve fast interfacial steps. Here we adopt this framework to quantify NH_3–H_2 competition on Fe(110) and to connect surface reaction kinetics to hydrogen-embrittlement outcomes. The bcc Fe(110) facet is the thermodynamically most stable (lowest surface free energy) over the stability range of bcc iron, and thus a commonly exposed and extensively studied model surface. It is routinely prepared and characterized as a clean single-crystal surface in UHV studies.

In this work, we use first-principle methods to investigate the co-adsorption of NH_3 and H_2 on the iron Fe(110) surface, including NH_3 molecular adsorption, NH_3 decomposition, and its competition with H_2 dissociation. We investigated the NH_3 adsorption rate and decomposition rate based on the transition state theory. Furthermore, we investigate the effect of preadsorbed NH_3 on the H_2 dissociation. Those processes are significant factors that control the NH_3 and H coverage on iron surface. We established a kinetic model to calculate the coverage of NH_3, NH_3-derived species, and H_2-derived H atoms on the Fe surface and investigated the NH_3 partial pressure effect on the NH_3-derived H atom coverage. In addition, we performed a fracture toughness test of JIS SCM440 Cr–Mo steel in H_2, NH_3 and H_2 mixture, NH_3 and N_2 mixture, and N_2 gases under gas pressure were 0.1 MPa in order to validate the calculation results. This material suffered from hydrogen embrittlement.

2. Methods of investigation

2.1 Theory

Periodic DFT was performed using Numerical Atomic Orbitals (NAO) implemented in Quantum ATK.[28] The method is based on quantum mechanics principles and can be used to investigate the structural and electronic properties of materials.[29] The GGA Perdew–Burke–Ernzerhof (PBE) exchange–correlation functional was applied using Fritz-Haber-Institute (FHI) pseudopotentials. Electron energies were converged to 10^{-6} eV using double zeta polarized (DZP) basis set for all valence electrons. All calculations were spin polarized. The calculations were performed with Monkhorst–Pack k-point mesh of $8 \times 8 \times 8$ (properly describe the properties of one unit cell for the BCC bulk iron lattice) and $4 \times 4 \times 1$ for the Fe(110) terminated iron

24590 | *Phys. Chem. Chem. Phys.*, 2025, **27**, 24589–24600

This journal is © the Owner Societies 2025

slab. The geometry relaxation was performed until the forces converged to values below 0.05 eV Å^{-1}. For bulk systems, relaxation was performed for the cell volume, cell shape, and atomic positions. For slab models, relaxation was performed for the atomic positions only. Slabs were constructed using 6 alternating iron layers. The coordinates of the atoms in the middle two layers were fixed, while the coordinates of the top two and bottom two were fully relaxed. Activation barriers for various reaction mechanisms were obtained using the climbing image-nudged elastic band method (CI-NEB). In the process of NEB calculations, eight to ten images were used between the starting and the ending geometries of reactions. Adsorption energies and activation barriers are reported as 0 K DFT total energies without free-energy corrections. This pragmatic approximation is widely used in surface reaction studies[30] (Exploring CO_2 hydrogenation to methanol at a CuZn–ZrO_2 interface *via* DFT calculations). These assumptions may not strictly hold for NH_3/H co-adsorption on Fe(110); however, within the coverage range examined (11–33%), this approximation is widely used and adequate for trend-level comparisons. Moreover, dissociative H_2 adsorption is treated with the standard $\sqrt{p(H_2)}$ dependence to reflect its two-site requirement. Coverage-dependent DFT energetics (Tables 3 and 5) partially account for lateral interactions by parameterizing rate/equilibrium constants at explicit coverages. Potential refinements (*e.g.*, Fowler–Guggenheim/Temkin isotherm) are discussed in the SI-S1.

In this study, the vibrational frequencies of normal modes of the decomposition reaction of NH_3 and dissociation reaction of H_2 were calculated by combining the dynamical matrix and vibrational mode calculation of Quantum ATK. Initial and transition geometry were converged to 10^{-8} eV to ensure that the vibrational frequency calculation yields proper results because vibrational frequency calculation requires well-converged electron density. Each ion in the cell is then displaced by ± 0.01 Å in all directions of the cartesian vector, then a Hessian matrix was constructed from the force which shows how atoms react to displacement. Force derivative tolerance is set to 10^{-3} eV Å^{-1}. Once the normal mode vibrational frequencies of the system were obtained, all data was (excluding the imaginary vibration of the transition state) divided by the product of the data from the initial geometry to obtain the attempt frequency.

$$A = \frac{\prod_{i=1}^{3N} v_i^{O}}{\prod_{i=1}^{3N} v_i^{S}} \quad (1)$$

where $\prod_{i=1}^{3N} v_i^{O}$ is multiplying all vibrational frequency at initial configuration, $\prod_{i=1}^{3N} v_i^{S}$ is multiplying all vibrational frequency at transition state configuration (has one more imaginary frequency).

2.2 Experiment

The material used in this study was JIS SCM440 Cr–Mo low-alloy steel. The chemical composition is shown in Table 1. The mechanical properties after the heat treatments are shown in Table 2. The microstructure was tempered martensite with BCC lattice. The fracture toughness tests were carried out in accordance with the ASTM E 1820 standard. The NH_3 partial pressure was 1000 ppm and 10 000 ppm. The loading rate was 2.0×10^{-3} and 2.0×10^{-5} mm s^{-1}. The temperature was 293 K. A detailed description of the fracture toughness test system and compact tension (CT) specimen is provided in the SI-S3. The authors have used the same test system to investigate the impurity mitigation effect on HE.

3. Result and discussion

3.1 Theory

We optimize the lattice of BCC iron and obtain a lattice constant of 2.82 Å, which agrees with previous reports in the literature.[30] The surface optimization yields a slightly shorter distance between the first and second layers and a slightly longer distance between the second and third layers. First, we investigate the surface geometry and surface coverage by NH_3 molecules. The Fe(110) surface provides three distinct adsorption positions for NH_3 molecules. Those positions include the top, bridge, and hollow sites. All initial geometries in the process of geometry optimization converge to top site of the Fe(110) surface as shown in Fig. 1. We used different quantities of NH_3 molecules to cover the Fe surface, representing different coverage as shown in Fig. 2. We examined the adsorption energy of NH_3 on Fe(110) to determine the effect of different surface coverages and it is summarized in Table 3. The adsorption energy of NH_3 on the Fe(110) surface decreases with the increase of NH_3 coverage. This phenomenon is based on two reasons: (1) the pre-adsorbed NH_3 withdrew and localized electron density of the Fe surface, thus the electron density of the adjacent sites is no longer sufficient for the additional NH_3 adsorption; (2) the repulsive interactions between the NH_3 molecules. The most stable surface geometry is NH_3 molecules occupying top sites with coverage in the range of 11–33%.

To fully understand the effect of NH_3 on HE we investigated the decomposition of NH_3 with a relatively low NH_3 coverage (11%) on Fe(110) surface as shown in Fig. 3 This NH_3 decomposition process consists of three distinct steps. During each
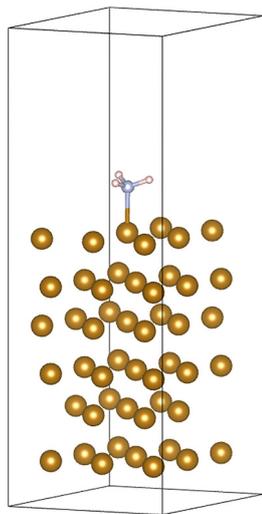
Table 1 Chemical composition of SCM440 (mass%)

Fe	C	Si	Mn	P	S	Cu	Ni	Cr	Mo
Bal.	0.40	0.22	0.63	0.008	0.004	0.02	0.02	0.94	0.15

Table 2 Mechanical properties of SCM440

0.2% proof strength (MPa)	Ultimate tensile strength (MPa)	Elongation	Reduction of area	Vickers hardness
841	971	20%	54%	HV329

This journal is © the Owner Societies 2025

Phys. Chem. Chem. Phys., 2025, **27**, 24589–24600 | **24591**

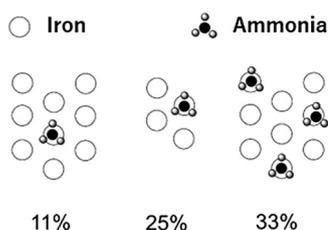Fig. 1 Optimized geometry of NH₃ molecule adsorption geometry.

Fig. 2 Schematic presentation of ammonia coverage on Fe 110 surface.

step, NH₃, NH₂, and NH will release a hydrogen atom on the iron surface. The products of the NH₃ and hydrogen decomposition occupied different sites on the surface and consequently affected the surface coverage as shown in Table 4. When gas molecules interact with surfaces, they establish equilibrium with the surface products which is governed by the adsorption law, the reaction kinetics, and the partial pressure of the gas components. An increase in the gas partial pressure leads to an increase in the coverage of the adsorption products on the solid surface at a constant temperature.[31–33] Therefore, to understand the effect of NH₃ partial pressure, a higher NH₃ coverage (25%) on the Fe(110) surface as shown in Fig. 4 (NH₃ decomposition on the iron surface at elevated coverage) was investigated. The summary of the activation energy barriers (E_a) of NH₃ decomposition in each step (initial geometry, transition geometry, and end geometry) is shown in Table 5. The E_a for the decomposition of NH₃ on the Fe(110) surface at 25% coverage is compared with that at 11% coverage. The first step of ammonia decomposition catalyzed by the Fe

surface is affected by an increase in the surface coverage of ammonia. Additionally, as ammonia molecules only interact with individual Fe atoms, the Fe surface provides sufficient electrons to catalyze the decomposition of ammonia. Consequently, the E_a for the first step decreases with increased NH₃ coverage. However, as NH₃ decomposes into NH₂ and NH, NH₂ and NH interact with two and three Fe atoms, respectively. This leads to the withdrawal and localization of more electrons, thereby reducing the available free electrons for catalysis. Therefore, both the second step (NH₂ → NH + H) and the third step (NH → N + H) of NH₃ decomposition exhibit significant changes with increased NH₃ coverage. The activation energy for the second decomposition step at 25% NH₃ coverage nearly doubles compared to that at 11% NH₃ coverage. Additionally, the reaction for the third decomposition step undergoes a transformation from an exothermic to an endothermic process as NH₃ coverage increases. Consequently, the higher NH₃ surface coverage mitigated NH₃ decomposition better.

We further investigate the H₂ dissociation process on the pure Fe(110) surface and Fe(110) surfaces pre-treated by NH₃ with different coverage. The geometries are summarized in Fig. 5. The activation energy barrier and dissociation energy of H₂ on the Fe(110) surface is shown in Table 6. Without NH₃ pre-adsorbed on the Fe(110) surface, the H₂ spontaneously dissociates on Fe(110) surface without an activation barrier. The dissociation energy of H₂ is −1.56 eV. At 11% coverage, the activation energy barrier for H₂ dissociation on Fe(110) surface is 0.04 eV, and the dissociation energy of H₂ is −1.54 eV. The dissociation energy slightly increased from 0.00 eV to 0.04 eV, which indicates that even at low coverage NH₃ can hinder H₂ dissociation. With the increase of NH₃ coverage on the Fe(110) surface from 11% to 33%, the activation barrier of H₂ dissociation increased up to 0.7 eV and the dissociation energy of H₂ decreased to −1.17 eV. The activation energy barrier would reduce the H₂ dissociation reaction rate. Decreasing the dissociation energy of H₂ would lead to easier H₂ molecule desorption. As a result, an increased activation energy barrier and decreased dissociation energy would lead to a decrease in the hydrogen atom concentration on the surface, thus, reducing the probability for hydrogen to permeate to Fe.

Chemical equilibrium is established by the mass fluxes between the gas phase and the surface equalize.[34] For molecules in contact with a solid surface at a fixed temperature, the Langmuir isotherm,[35] describes the partitioning between the gas phase and adsorbed species as a function of applied pressure. The basic assumption of this theory is: (1) assume the surface is homogeneous (no corrugations); (2) all sites are energetically equivalent, and the energy of adsorption is equal for all sites; (3) the gas adsorbs into an immobile state; (4) mono-layer coverage only; (5) no interactions between

Table 3 Adsorption energy of NH₃ on Fe 110 surface for different coverage

Coverage	11% NH₃ adsorbed on Fe(110)	25% NH₃ adsorbed on Fe(110)	33% NH₃ adsorbed on Fe(110)
Adsorption energy (eV)	−1.01	−0.94	−0.93

24592 | *Phys. Chem. Chem. Phys.*, 2025, **27**, 24589–24600

This journal is © the Owner Societies 2025
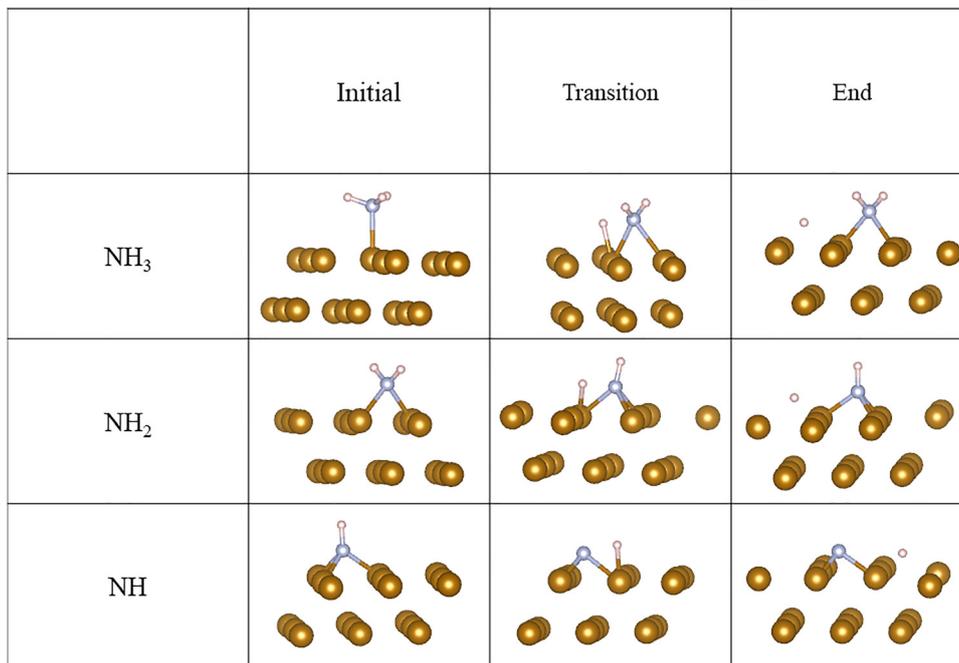
Fig. 3 NH$_3$-derived hydrogen atom on Fe(110) surface (11%).

Table 4 Occupied site of different adsorbed species on Fe(110) surface

Adsorbed species	Occupied site
NH$_3$	Top
NH$_2$	Bridge
H atom derived by NH$_3$	Bridge
NH	Hollow
H atom derived by NH$_2$	Bridge
N	Hollow
H atom derived by NH	Bridge

adsorbate molecules on adjacent sites.[36,37] The Langmuir theory consisted of different adsorption models: adsorption, competitive adsorption, dissociative adsorption, and competitive and dissociative adsorption. In this study, we investigate the competitive and dissociative adsorption of NH$_3$ and H$_2$ on the Fe(110) surface. Because NH$_3$–H$_2$ co-adsorption shows coverage effects, we benchmarked our conclusions against an interaction-inclusive isotherm following Christensen *et al.*;[38] details and sensitivity results are in SI-S1.

For the single adsorbate case, the model assumes adsorption and desorption as being elementary processes, where the rate of adsorption r_{ad} and the rate of desorption r_d are given by

$$r_{ad} = k_{ad}p_A[S] \tag{2}$$

$$r_d = k_d[A_{ad}] \tag{3}$$

where p_A is the partial pressure of A over the surface, [S] is the surface concentration of the free site, [A$_{ad}$] is the surface concentration of adsorbed specie A, and the k_{ad} and k_d are the constants of forward adsorption reaction, and backward desorption reaction in the above reaction.

At equilibrium, the rate of adsorption is equal to the rate of desorption. Setting $r_{ad} = r_d$, thus, the equilibrium constant

$$K_{eq}^A = \frac{[A_{ad}]}{p_A[s]} = \frac{k_{ad}}{k_d} \tag{4}$$

In eqn (4), the rate is given by the Arrhenius equation.[39] The equilibrium constant is independent of the pressure of the system or of the concentration of the reacting species. If the entire surface is covered by adsorbed species A and free sites, and we apply eqn (4) we can derive the Langmuir adsorption isotherm,

$$\theta_A = \frac{P_A K_A}{1 + P_A K_A} \tag{5}$$

For competitive adsorption, the surface is covered by A, B, and free sites, therefore, the expressions for adsorbed species of A and B in surface coverage θ_A and θ_B are as follows:

$$\theta_A = \frac{P_A K_A}{1 + P_A K_A + P_B K_B} \tag{6}$$

$$\theta_B = \frac{P_B K_B}{1 + P_A K_A + P_B K_B} \tag{7}$$

However, in the case of dissociation adsorption, the 1/2 power on p_{D_2} arises because one gas phase molecule produces two adsorbed species.

In this study, we have performed surface coverage estimation based on the Langmuir theory. The Langmuir model neglects explicit adsorbate–adsorbate interactions and spatial correlations; such effects can matter when co-adsorbates interact or when pair-site requirements apply, and more detailed
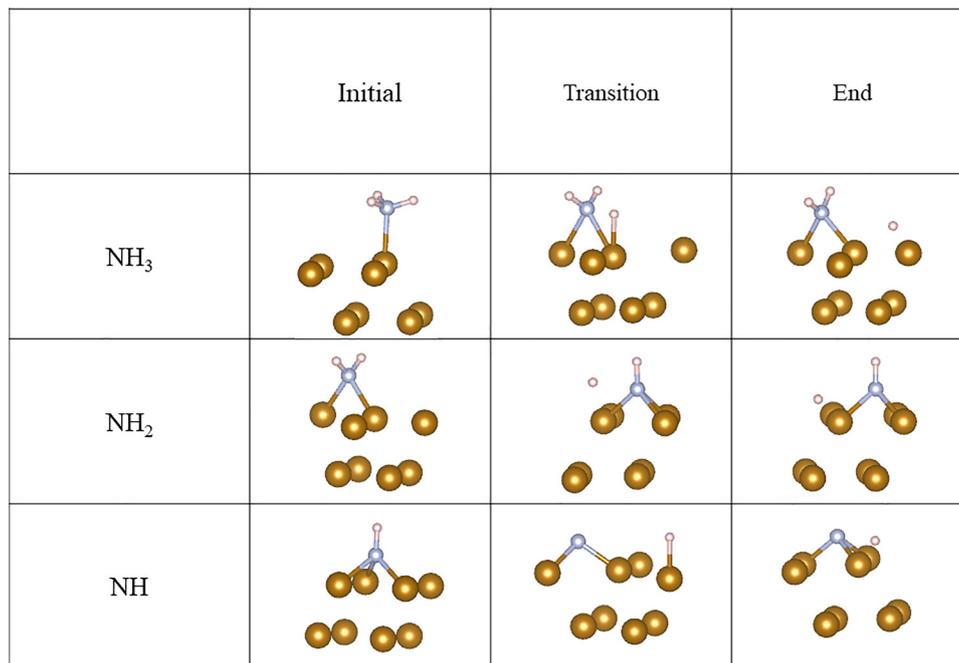
This journal is © the Owner Societies 2025

Phys. Chem. Chem. Phys., 2025, **27**, 24589–24600 | **24593**

	Initial	Transition	End
NH$_3$			
NH$_2$			
NH			

Fig. 4 NH$_3$-derived hydrogen atom on Fe(110) surface (25%).

Table 5 Decomposition and desorption E_a of NH$_3$ on Fe(110) surface

	Decomposition activation barrier (11%)	Decomposition activation barrier (25%)	Desorption activation barrier (11%)	Desorption activation barrier (25%)
NH$_3$ → NH$_2$ + H	0.72 eV (Exo)	0.68 eV (Exo)	1.43 eV (Endo)	1.39 eV (Endo)
NH$_2$ → NH + H	0.45 eV (Exo)	0.84 eV (Exo)	1.36 eV (Endo)	1.70 eV (Endo)
NH → N + H	0.99 eV (Exo)	1.05 eV (Endo)	1.18 eV (Endo)	0.98 eV (Exo)

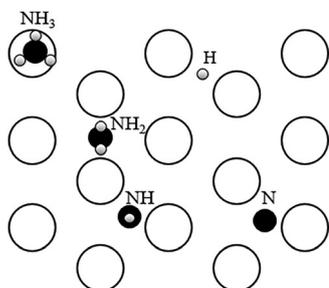Exo = exothermic reaction. Endo = endothermic reaction.

Fig. 5 Schematic presentation of adsorbate position on Fe 110 surface.

treatments (Fowler–Guggenheim/Temkin, cluster/Monte-Carlo or pair-site LH variants) may be used when needed. Here our objective is to rationalize relative trends; under these conditions, mean-field microkinetics remains a standard and defensible baseline. The H$_2$ molecule dissociates into two H atoms and can be solved by the 1/2 power on p_{H_2}. The complete NH$_3$ decomposition on the Fe surface is into an N atom and three H atoms. The kinetic derivation of NH$_3$ complete decomposition on the Fe surface, and complete NH$_3$ decomposition competitive with H$_2$ dissociation on the Fe surface are studied after considering NH$_3$ adsorbed on Fe(110) surface as a single molecule.

3.2 NH$_3$ mitigation effect on HE

To investigate the mechanism of NH$_3$ mitigation effect on HE, we first considered the NH$_3$ adsorbed on the Fe surface as a

Table 6 Dissociation energy of H$_2$

Coverage	0% NH$_3$ pre-adsorb Fe(110)	11% NH$_3$ pre-adsorb Fe(110)	25% NH$_3$ pre-adsorb Fe(110)	33% NH$_3$ pre-adsorb Fe(110)
Activation energy (eV)	0.00	0.04	0.06	0.07
Dissociation energy (eV)	−1.56	−1.54	−1.22	−1.17

24594 | *Phys. Chem. Chem. Phys.*, 2025, **27**, 24589–24600

This journal is © the Owner Societies 2025

molecule (without decomposition) and performed the Langmuir adsorption model, which assumes the adsorbate behaves as an ideal gas under isothermal conditions.[39–41] We apply the Langmuir competitive adsorption model in eqn (6) and (7), and further extend it to competitive and dissociative model due to H₂ is dissociative adsorption on the Fe surface. The 1/2 power on H₂ arises because hydrogen atoms occupy two sites on the surface. We used the data in Tables 5 and 6 to modify the Langmuir competitive adsorption model for the NH₃ and H₂ competitive and dissociative co-adsorption on the Fe(110) surface. The surface coverage equation for NH₃ adsorption and H₂ dissociative adsorption is given below (eqn (8) and (9), respectively). In those equations, θ_{NH_3} and θ_H are denoted by the fractional occupancy on the surface by NH₃ or atomic hydrogen, respectively. The activation barriers for different NH₃ coverage are taken from the DFT calculations, the temperature is set to 293 K, and high-purity H₂ was considered with 1000 ppm and 10 000 ppm partial pressure of NH₃ to match the experiment conditions. We used two different coverage models to represent the different NH₃ partial pressure on H₂ gas because increased partial pressure leads to higher surface coverage.[42,43] Thus, 1 NH₃ on the 9 surface Fe model represents the lower partial pressure of NH₃ in H₂, and 1 NH₃ on the 4 surface Fe model represents the higher partial pressure of NH₃ in H₂.

$$\theta_{NH_3} = \frac{P_{NH_3}K_{NH_3}}{1 + P_{NH_3}K_{NH_3} + \sqrt{P_{H_2}K_{H_2}}} \quad (8)$$

$$\theta_H = \frac{\sqrt{P_{H_2}K_{H_2}}}{1 + P_{NH_3}K_{NH_3} + \sqrt{P_{H_2}K_{H_2}}} \quad (9)$$

In eqn (8) and (9) K_{NH_3} and K_{H_2} denote the NH₃ and H₂ adsorption/desorption equilibrium constants for activation barriers listed in Tables 5 and 6, which were calculated by DFT. P_{NH_3} and P_{H_2} denote the partial pressure of NH₃ and H₂, respectively. The rate constants were estimated using the Arrhenius equation, where A is a preexponential factor, R is the gas constant, T is the temperature, and E_a is the activation barrier. The equilibrium constants are computed as the ratio between the adsorption and the desorption rate constants. The preexponential factor is computed as the reaction attempt frequency which is given by the product of the vibration frequencies at the resting site divided by the product of vibration frequencies in the transition state (the single imaginary frequency is excluded). It is important to note that the preexponential factor differs for the forward and reversed reactions. While the vibration frequencies at transition state are the same, they differ for the starting and end point of the reaction (product and reactant). The vibration frequencies are obtained through Hessian deionization in the DFT calculations.

From the cooperative adsorption/desorption/dissociation model in eqn (8) and (9), we calculated the NH₃ and atomic hydrogen coverage on the Fe surface with different NH₃ partial pressure, the result is shown in Table 7. The hydrogen atom coverage on the Fe(110) surface is decreasing with the increase

Table 7 Coverage of NH₃ and atomic hydrogen on Fe(110) surface non-dissociative NH₃

Condition	H₂ + 1000 ppm NH₃	H₂ + 10 000 ppm NH₃
θ_{NH_3}	10%	25%
θ_H	1.70%	0.01%

in NH₃ coverage, which is achieved by increased NH₃ partial pressure. There is no direct study related to the ratio of atomistic hydrogen surface coverage on iron surface and initiation of crack growth induced by HE. We have reported that hydrogen atom coverage on the iron surface is 0.6% with CO 75% coverage.[16] Experimental results show that CO could mitigate the HE.[16] For NH₃ 25% coverage on Fe(110) surface the atomic hydrogen coverage is 0.01%, which is below 0.60%. Thus, we can expect that NH₃ could possibly mitigate HE if it could have a faster adsorption rate compared to H₂.

Surface reactions can be classified into two generic types. The first includes reactions between two adsorbed species or between an adsorbed species and a vacant site (Langmuir–Hinshelwood process), which is fitting for our consideration of coadsorption between NH₃ and H₂. The other reaction is called the Eley–Rideal process, which is considering that adsorbed species form a product.

Based on the Langmuir–Hinshelwood process, for randomly distributed adsorbates on a surface in the absence of adsorbate-adsorbate interactions, the rate of reaction is given by eqn (10).

$$r_r = k\theta_A\theta_v \quad (10)$$

$$k = Ae^{-\frac{E_a}{RT}} \quad (11)$$

where θ_A is the surface coverage of species A, and θ_v is the fraction of the vacant sites. We calculated the pre-exponential factor (frequency factor) of NH₃ and H₂ using DFT frequency calculations (see eqn (1)) for calculating their reaction rate coefficient (eqn (11)). Table 8 shows the pre-exponential factors, reaction rate coefficient, and reaction rate of NH₃ and H₂ on the Fe(110) surface. The reaction rate coefficient of NH₃ and H₂ on the Fe(110) surface is based on eqn (10). We use the computed pre-exponential factors and activation energies for NH₃ and hydrogen from Table 8 to estimate the equilibrium constants for NH₃ and hydrogen adsorption/desorption on Fe(110) surface. Then, we use those equilibrium constants in eqn (10) and (11) with the NH₃ partial pressure for 1000 ppm and 10 000 ppm to estimate the hydrogen and NH₃ reaction rates in Table 8.

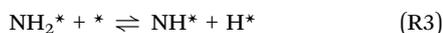**Table 8** Pre-exponential factor, reaction rate coefficient, and reaction rate of NH₃ and H₂

	NH₃	H₂
A (Hz)	3.18×10^{20}	3.90×10^{11}
k (s⁻¹)	3.14×10^{20}	3.92×10^{11}
$r_{r(11\%NH_3)}$ (s⁻¹)	2.77×10^{19}	5.85×10^9
$r_{r(25\%NH_3)}$ (s⁻¹)	5.88×10^{19}	2.92×10^7

This journal is © the Owner Societies 2025

Phys. Chem. Chem. Phys., 2025, **27**, 24589–24600 | **24595**

With increasing the coverage of NH$_3$ from 11% to 25%, the reaction rate of H$_2$ with the Fe(110) surface decreases from 5.85×10^9 s^{-1} to 2.92×10^7 s^{-1}. Thus, increasing NH$_3$ partial pressure reduces hydrogen dissociation rate on Fe(110) surface. On the other hand, the adsorption rate of NH$_3$ is significantly faster than H$_2$, which indicates that NH$_3$ preferentially adsorbs on the Fe(110) surface compared to H$_2$.

3.3 Effect of NH$_3$ decomposition on its mitigation effect on HE (while competing with H$_2$ dissociation)

To fully understand the effect of NH$_3$ competing with H$_2$ with respect to HE, we divided the process of NH$_3$ decomposition into four steps, and simultaneously considered the dissociation of H$_2$. The decomposition mechanism of NH$_3$ includes the chemisorption of NH$_3$ on the catalyst surface,[40,43–46] stepwise dehydrogenation of NH$_3$ to NH$_2$ + H, NH + H, N + H. The adsorption of all the species follows the Langmuir isotherm model, therefore it is assumed that the surface sites are energetically equivalent, and each site can hold at most one adsorbed species. The mechanism can be described according to the following sequence of elementary reactions as shown in (R1)–(R4):

$$NH_3 + * \rightleftharpoons NH_3* \quad \text{(R1)}$$

$$NH_3* + * \rightleftharpoons NH_2* + H* \quad \text{(R2)}$$

$$NH_2* + * \rightleftharpoons NH* + H* \quad \text{(R3)}$$

$$NH* + * \rightleftharpoons N* + H* \quad \text{(R4)}$$
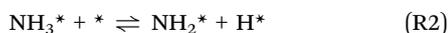
To establish the kinetic model of competitive and dissociative co-adsorption between NH$_3$ and H$_2$ on the Fe(110) surface we must consider the H$_2$ dissociation. The reaction of H$_2$ dissociation on the Fe(110) surface can be expressed by the chemical reaction (R5) below:

$$H_2 + 2* \rightleftharpoons 2H* \quad \text{(R5)}$$

The term * denotes a vacant site, and NH$_3$*, NH$_2$*, NH*, N*, and H* are the adsorbed species. NH$_3$ and H$_2$ represent the free gaseous state. If all the above reactions are equilibrium that the constants of equilibrium (K_1, K_2, K_3, K_4, and K_5) are given by eqn (3) for each step. The reaction rate coefficient k

$\left(\overrightarrow{k_1}, \overleftarrow{k_1}, \overrightarrow{k_2}, \overleftarrow{k_2}, \overrightarrow{k_3}, \overleftarrow{k_3}, \overrightarrow{k_4}, \overleftarrow{k_4} \right)$ in each step is given by Arrhenius equation (eqn (11)).

Then, we investigate the hydrogen atom surface coverage from the NH$_3$ decomposition on the Fe(110) surface step by step and compare the competing H$_2$ dissociation reaction. We assume that the reaction stops at each step and reaches equilibrium. Therefore, the whole process is divided into three cases denoted with 1, 2, and 3.

In order to keep the main text concise, we only summarize the setup of the staged NH$_3$ decomposition while competing with H$_2$ dissociation. We analyze three quasi-equilibrated stopping cases—Case 1 (NH$_3$* $\rightleftharpoons$ NH$_2$* + H*), Case 2 (up to NH* + H*), and Case 3 (up to N* + H*)—with competitive dissociative H$_2$ adsorption (H$_2$ + 2* $\rightleftharpoons$ 2H*). The corresponding equilibrium relations (K_1–K_5), Arrhenius parameterization, and the site balance are solved self-consistently at 293 K under the stated gas compositions. The full mass-balance equations, algebraic solution, and numerical procedure are provided in SI-S2, and the resulting coverages are reported in Table 9.

The hydrogen coverage of each case is summarized in Table 9. From Case 1 to Case 3, owing to the NH$_3$ decomposition, the hydrogen atom coverage on Fe(110) surface significantly increased from 2.96% to 8.42% (1000 vppm NH$_3$), 4.73% to 15.20% (10 000 vppm NH$_3$). The hydrogen atom coverage on Fe(110) surface increased with the NH$_3$ decomposition and the NH$_3$ partial pressure. The final step of NH$_3$ decomposition to N and H has almost no contribution to H atom coverage on the Fe surface. However, the HE mitigation effect is not only affected by coverage, but also time dependent through the reaction rate. Therefore, we investigate the decomposition rate of NH$_3$ at each step.

We use the Arrhenius equation (eqn (11)) where the pre-exponential factor A is taken from Table 8, the E_a is taken from Table 5, R is the universal gas constant, and T is 293 K for fitting with the fracture toughness test condition. The reaction rate coefficient of NH$_3$ decomposition in each step can be calculated as shown in Table 10. Under the same NH$_3$ partial pressure, the reaction rate coefficient of NH$_3$, NH$_2$, and NH is decreasing. For lower NH$_3$ partial pressure (1000 vppm) we find a reduction in the reaction rate coefficient from NH$_2$ to NH, which demonstrates that the last step of NH$_3$ decomposition (NH $\rightarrow$ N + H) is the slowest step. However, the first two decomposition steps (NH$_3$ $\rightarrow$ NH$_2$ + H; NH$_2$ $\rightarrow$ NH + H) are characterized with high reaction rate coefficients. When the NH$_3$ partial pressure is increased to 10 000 vppm we find a reduction in the reaction rate coefficient from NH$_3$ to NH$_2$, which indicates that the NH$_3$ decomposition is not likely to occur on the experimental time scale. Thus, during the experimental time scale, increased NH$_3$ partial pressure will decrease the NH$_3$ decomposition rate

Table 9 Summary of hydrogen coverage on Fe(110) surface

	H coverage 1000 vppm NH$_3$ + H$_2$	H coverage 10 000 vppm NH$_3$ + H$_2$
Case 1	2.96%	4.37%
Case 2	8.42%	15.20%
Case 3	8.42%	15.20%

Table 10 Reaction rate coefficient k of NH$_3$ decomposition

	NH$_3$	NH$_2$	NH
k (1000 vppm NH$_3$) (s^{-1})	1.368×10^8	7.284×10^5	2.130×10^{-1}
k (10 000 vppm NH$_3$) (s^{-1})	6.656×10^8	1.459×10^{-1}	1.986×10^{-2}

24596 | *Phys. Chem. Chem. Phys.*, 2025, **27**, 24589–24600

This journal is © the Owner Societies 2025

constant, and in a limited time scale, before the equilibrium is reached, it might successfully kinetically mitigate HE.

Our theoretical results at equilibrium show that the hydrogen coverage on Fe(110) surface increases with the increase in NH$_3$ partial pressure. However, the NH$_3$ reaction kinetics suggests that at short time intervals NH$_3$ will decompose to NH$_2$, NH and H at low partial pressure (1000 vppm) and only to NH$_2$ and H at high partial pressure (10 000 vppm). Thus, the H surface coverage will be kinetically locked to 8.42% at 1000 vppm NH$_3$ partial pressure and 4.37% at 10 000 vppm NH$_3$ partial pressure. As a result, increasing the NH$_3$ partial pressure would have a mitigating effect on HE.

4. Fracture toughness test results

Hydrogen embrittlement is a phenomenon that includes a series of processes: surface adsorption/desorption, molecular dissociation, surface/sub-surface migration, hydrogen dissolution, defects trapping, grain boundaries segregation, hydrogen concentration ahead of the crack tip, *etc.* In this study, we designed an experiment where we kept all conditions the same and attempted to only relate the crack growth resistance ability of the material to the ammonia partial pressure and loading rate.

The fracture toughness test results, shown in Fig. 6, illustrate the relationship between the *J*-integral value and crack extension (Δa). The fracture toughness of the material, determined by the *J*-integral value at the intersection of the J–Δa curve and the 0.2 mm offset line, is evaluated in accordance with the ASTM E1820 standard. This value represents the material's resistance to the onset of crack extension. The data obtained in high-purity N$_2$ serves as the reference.

At the loading rate was 2.0×10^{-3} mm s^{-1}, there was a reduction of fracture toughness of material in H$_2$ gas. This result indicates that hydrogen embrittlement occurred. However, when 1000 ppm NH$_3$ is added to H$_2$ gas, the reduction is recovered. It was confirmed that NH$_3$ has a mitigating effect on

hydrogen embrittlement. The NH$_3$ mitigation effect increased with increased NH$_3$ partial pressure.

Additionally, we conducted fracture toughness tests in nitrogen gas with added NH$_3$. If NH$_3$ has neither a detrimental nor an improving effect, it is expected that the J–Δa curve would match that obtained in pure N$_2$. During the fracture toughness test with 1000 ppm NH$_3$ at a loading rate of 2.0×10^{-3} mm s^{-1}, no reduction in fracture toughness was observed. However, surprisingly, when the loading rate was reduced to 1/100 (*i.e.*, 2.0×10^{-5} mm s^{-1}), the J–Δa curve for nitrogen gas with 1000 ppm NH$_3$ shifted significantly downward, resulting in a marked decrease in fracture toughness.

As shown in Fig. 7, the fracture surface obtained in nitrogen gas with 1000 ppm NH$_3$ exhibited a quasi-cleavage fracture morphology, resembling the fracture surface obtained in the fracture toughness test in hydrogen. This observation suggests that hydrogen embrittlement occurred despite the absence of H$_2$ gas in the test environment. A possible mechanism is the production of hydrogen atoms due to the decomposition of NH$_3$ on the iron surface, facilitated by the catalytic action of the Fe surface (Fig. 8).

In summary, NH$_3$ exhibits both mitigating and inducing effects on hydrogen embrittlement, depending on the loading rate. If this assumption is correct, the loading rate dependence of NH$_3$'s mitigating effect in H$_2$ + NH$_3$ environments can be clearly explained. As shown in Fig. 7, the addition of 1000 ppm NH$_3$ significantly mitigated HE at a loading rate of 2×10^{-3} mm s^{-1}. However, this mitigating effect drastically diminished when the loading rate was reduced to 2×10^{-5} mm s^{-1}.
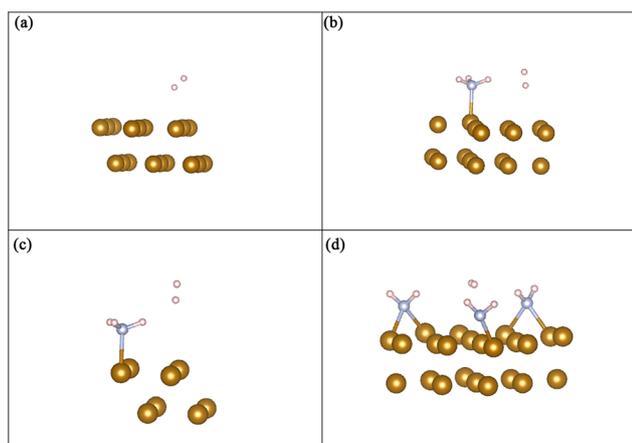

Fig. 6 Molecular hydrogen dissociation on the Fe(110) surface with (a) 0%, (b) 11%, (c) 25%, and (d) 33% NH$_3$ coverage.
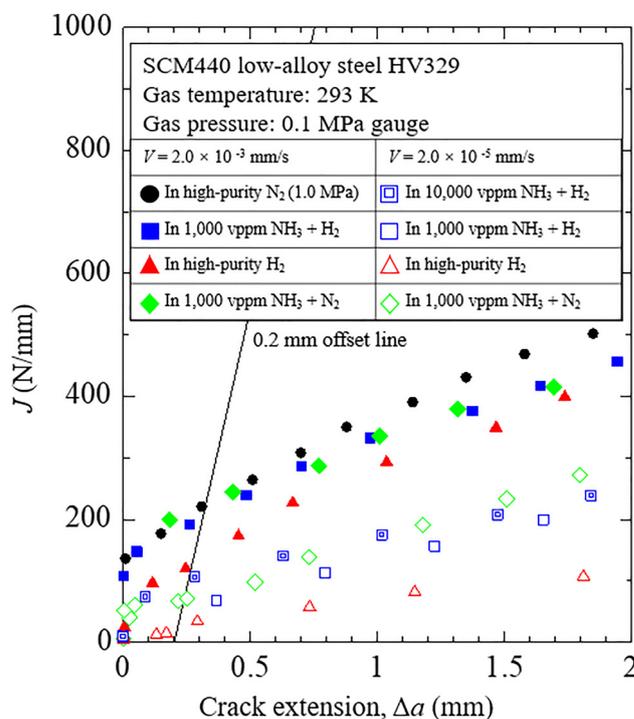

Fig. 7 Mitigation effect of NH$_3$ on HE and its loading rate and concentration dependency.
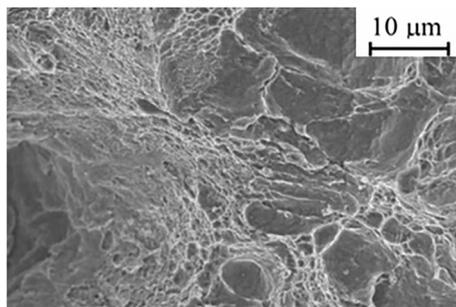
This journal is © the Owner Societies 2025

Phys. Chem. Chem. Phys., 2025, **27**, 24589–24600 | **24597**

Fig. 8 Fracture surface tested in 1000 ppm NH$_3$ + N$_2$.

According to the DFT simulation results shown in Table 8 and 10, the adsorption rate of NH$_3$ on the Fe surface is significantly higher than its decomposition rate. Therefore, at a relatively high loading rate, crack propagation occurs while the Fe surface is predominantly covered by NH$_3$ molecules, suppressing hydrogen uptake into the material. In contrast, at a sufficiently low loading rate, the slower crack propagation allows NH$_3$ to decompose into H and NH$_2$. The hydrogen produced from NH$_3$ decomposition then becomes a source of hydrogen embrittlement, negating the mitigating effect of NH$_3$.

However, Fig. 7 still presents a puzzling result. Specifically, in the fracture toughness test conducted at a loading rate of 2.0×10^{-5} mm s^{-1}, the fracture toughness in the 10 000 ppm NH$_3$ + H$_2$ environment was higher than that in the 1000 ppm NH$_3$ + H$_2$ environment. If the previous discussion—that NH$_3$ decomposition produces hydrogen atoms at relatively low loading rates—is correct, it would be expected that increasing the NH$_3$ concentration would further reduce fracture toughness due to an increase in hydrogen atom production. However, the observed result is the opposite.

This anomaly can be explained by the results of the DFT calculations shown in Table 10. As shown in the figure, the NH$_3$ decomposition rate (NH$_2$ → NH + H) dramatically decreases with increasing NH$_3$ partial pressure. This is because NH$_3$ decomposition requires a vacant site adjacent to the adsorbed NH$_3$ on the Fe surface. An increase in NH$_3$ concentration leads to higher surface coverage of NH$_3$ on the Fe surface, thereby reducing the availability of vacant sites. Consequently, the adsorbed NH$_3$ loses the opportunity to decompose as the NH$_3$ concentration increases.

5. Conclusion

NH$_3$ was preferentially adsorbed on the Fe(110) surface because the adsorption rate of NH$_3$ on the Fe(110) surface is significantly higher than H$_2$. When the coverage of NH$_3$ on the Fe(110) surface was 25%, the atomic hydrogen coverage on Fe(110) surface would be 0.01%. In conclusion, preferentially adsorbed NH$_3$ mitigates the HE in gaseous hydrogen by hindering hydrogen uptake. The NH$_3$ decomposition reaction has a strong time dependence because the adsorption rate of NH$_3$ is much higher than its decomposition rate. Therefore, NH$_3$ decomposition occurs only when reaction time is sufficient. The NH$_3$

decomposition rate (NH$_2$ → NH + H) decreased as NH$_3$ partial pressure increased resulting in hindering NH$_3$-derived hydrogen supply. As a result, insufficient time for NH$_3$ further decomposition leads to lower H atom coverage on the Fe surface even at high NH$_3$ partial pressures. Therefore, increased NH$_3$ partial pressure could successfully mitigate HE through a kinetic mechanism. Our fracture toughness test results supported the theoretical results well. The test duration was controlled by the loading rate. Under the relatively higher loading rate, NH$_3$ mitigates HE. However, as we reduced the loading rate, the NH$_3$ mitigation effect on HE decreased due to its decomposition. Under the relatively slower loading rate, the NH$_3$ mitigation effect increased with increased NH$_3$ partial pressure. This kinetic modeling highlights two practical control parameters for hydrogen entry: NH$_3$ surface coverage (*via* partial pressure) and exposure time scale (loading rate). At high coverage and short times, rapid NH$_3$ adsorption suppresses H$_2$ dissociation; over longer times, slow NH$_3$ decomposition can supply H to the surface. These findings suggest pressure–time operating windows to limit hydrogen ingress and offer a transferable protocol for HE mitigation strategy.

Conflicts of interest

There are no conflicts to declare.

Data availability

The manuscript contains the computed results and detailed explanation how the simulations can be repeated and verified. In addition, supplementary information (SI) file is provided containing description of the experimental setup. In case further information is needed, it can be obtained *via* email from the corresponding author. Supplementary information is available. See DOI: **https://doi.org/10.1039/d5cp02423d**.

Acknowledgements

References

1 D. Hardie and P. McIntyre, The low-temperature embrittlement of niobium and vanadium by both dissolved and precipitated hydrogen, *Metall. Trans. A*, 1973, **4**, 1247–1254.
2 A. R. Troiano, The role of hydrogen and other interstitials in the mechanical behavior of metals, *Trans. Am. Soc. Met.*, 1960, **52**, 54–80.

24598 | *Phys. Chem. Chem. Phys.*, 2025, **27**, 24589–24600

This journal is © the Owner Societies 2025

3 H. K. Birnbaum and P. Sofronis, Hydrogen-enhanced localized plasticity—a mechanism for hydrogen-related fracture, *Mater. Sci. Eng., A*, 1994, **176**, 191–202.

4 C. D. Beachem, A new model for hydrogen-assisted cracking (hydrogen "embrittlement"), *Metall. Trans.*, 1972, **3**, 441–455.

5 S. Suresh and R. O. Ritchie, Mechanistic dissimilarities between environmentally influenced fatigue-crack propagation at near-threshold and higher growth rates in lower strength steels, *Mater. Sci.*, 1982, **16**, 529–538.

6 D. Hardie and S. Liu, The effect of stress concentration on hydrogen embrittlement of a low alloy steel, *Corros. Sci.*, 1996, **38**, 721–733.

7 H. E. Townsend, Effects of zinc coatings on the stress corrosion cracking and hydrogen embrittlement of low-alloy steel, *Metall. Mater. Trans. A*, 1975, **6**, 877–883.

8 P. S. Lam, R. L. Sindelar, A. J. Duncan and T. M. Adams, Literature Survey of Gaseous Hydrogen Effects on the Mechanical Properties of Carbon and Low Alloy Steels, *J. Press Vessel. Technol.*, 2009, **131**, 1–14.

9 R. P. Gangloff, Gaseous hydrogen embrittlement of high strength steels, *Metall. Mater. Trans. A*, 1977, **8**, 1043–1053.

10 B. P. Somerday, P. Sofronis and K. A. Nibur, *et al.*, Elucidating the variables affecting accelerated fatigue crack growth of steel in hydrogen gas with low oxygen concentrations, *Acta Mater.*, 2013, **61**, 6153–6170.

11 R. Komoda, K. Yamada and M. Kubota, *et al.*, The inhibitory effect of carbon monoxide contained in hydrogen gas environment on hydrogen-accelerated fatigue crack growth and its loading frequency dependency, *Int. J. Hydrogen Energy*, 2019, **44**, 29007–29016.

12 A. Staykov, J. Yamabe and B. P. Somerday, Effect of hydrogen gas impurities on the hydrogen dissociation on iron surface, *Int. J. Quantum Chem.*, 2014, **114**, 626–635.

13 A. Staykov, R. Komoda and M. Kubota, *et al.*, Coadsorption of CO and H$_2$ on an Iron Surface and Its Implication on the Hydrogen Embrittlement of Iron, *J. Phys. Chem. C*, 2019, **123**, 30265–30273.

14 R. Komoda, M. Kubota and S. Yoshida, *et al.*, Inhibition of Hydrogen Embrittlement of Cr-Mo Steel by the Addition of Impurities to Hydrogen Environment and the Effect of Material Strength. *Paper presented at the The 28th International Ocean and Polar Engineering Conference*, Sapporo, Japan, June 2018.

15 R. Komoda, M. Kubota and A. Staykov, *et al.*, Inhibitory effect of oxygen on hydrogen-induced fracture of A333 pipe steel, *FFEMS*, 2019, **42**, 1387–1401.

16 J. H. Holbrook, H. J. Cialone and E. W. Collings, *et al.*, Control of hydrogen embrittlement of metals by chemical inhibitors and coatings, in *Woodhead Publishing Series in Metals and Surface Engineering, Gaseous Hydrogen Embrittlement of Materials in Energy Technologies*, ed. R. P. Gangloff and B. P. Somerday, Woodhead Publishing, 2012, ch. 5, vol. 1, pp. 129–153.

17 A. Nagao, J. Koga, S. Takagi, H. Ono and N. Ishikawa, *Experimental and computational studies on hydrogen entry into steel exposed to high-pressure hydrogen gas*, ISIJ conference, Tokyo, Japan, 2018.

18 F. Bakhshi and N. Farhadian, Co-doped graphene sheets as a novel adsorbent for hydrogen storage: DFT and DFT-D3 correction dispersion study, *Int. J. Hydrogen Energy*, 2018, **43**, 8355–8364.

19 A. Staykov, J. Yamabe and B. P. Somerday, Effect of hydrogen gas impurities on the hydrogen dissociation on iron surface, *Int. J. Quantum Chem.*, 2014, **114**, 626–635.

20 B. P. Somerday, P. Sofronis and K. A. Nibur, *et al.*, Elucidating the variables affecting accelerated fatigue crack growth of steel in hydrogen gas with low oxygen concentrations, *Acta Mater.*, 2013, **61**, 6153–6170.

21 A. Staykov, R. Komoda and M. Kubota, *et al.*, Coadsorption of CO and H$_2$ on an Iron Surface and Its Implication on the Hydrogen Embrittlement of Iron, *J. Phys. Chem. C*, 2019, **123**, 30265–30273.

22 G. T. Gunasooriya, *et al.*, CO Adsorption on Pt(111): From Isolated Molecules to Ordered High-Coverage Structures, *ACS Catal.*, 2018, **8**, 10225–10233.

23 C. Samanta, Direct synthesis of hydrogen peroxide from hydrogen and oxygen: An overview of recent developments in the process, *Appl. Catal., A*, 2008, **350**, 133–149.

24 A. Manasilp and E. Gulari, Selective CO oxidation over Pt/alumina catalysts for fuel cell applications, *Appl. Catal., B*, 2002, **37**, 17–25.

25 V. Srikrishnan, Selective adsorption and hydrogen embrittlement, *Metall. Mater. Trans. A*, 1976, **11**, 1669–1675.

26 G. T. Gunasooriya, *et al.*, CO Adsorption on Pt(111): From Isolated Molecules to Ordered High-Coverage Structures, *ACS Catal.*, 2018, **8**, 10225–10233.

27 M. R. Louthan and R. E. Swanson, Material defects, gas purity and hydrogen embrittlement, *Int. J. Hydrogen Energy*, 1985, **10**, 551–554.

28 S. Smidstrup and T. Markussen, *et al.*, Quantum ATK: an integrated platform of electronic and atomic-scale modelling tools, *J. Phys. Condens.*, 2019, **32**, 1–36.

29 J. R. Chelikowsky and S. G. Louie, First-principles linear combination of atomic orbitals method for the cohesive and structural properties of solids: application to diamond, *Phys. Rev. B: Condens. Matter Mater. Phys.*, 1984, **29**, 6–15.

30 J. A. Yan, C. Y. Wang and S. Y. Wang, Generalized-stacking-fault energy and dislocation properties in bcc Fe: a first-principles study, *Phys. Rev. B: Condens. Matter Mater. Phys.*, 2000, **70**, 1–5.

31 G. M. Hermse and F. Frechard, *et al.*, Combining density-functional calculations with kinetic models: NO/Rh(111), *J. Chem. Phys.*, 2003, **118**, 7081–7089.

32 F. Mafuné, J. M. Bakker and S. Kudoh, Dissociative adsorption of NO introduces flexibility in gas phase Rh^{6+} clusters leading to a rich isomeric distribution, *Chem. Phys. Lett.*, 2021, **780**, 138937.

33 M. H. John and T. Ziegler, Density Functional Theory and Kinetic Studies of Methanation on Iron Surface, *J. Phys. Chem. C*, 2007, **111**, 11012–11025.

This journal is © the Owner Societies 2025

Phys. Chem. Chem. Phys., 2025, **27**, 24589–24600 | **24599**

34 M. W. Lindauer, The evolution of the concept of chemical equilibrium from 1775 to 1923, *J. Chem. Educ.*, 1962, **39**, 384–390.

35 I. Langmuir, The Adsorption of Gases on Plane Surface of Glass, Mica and Platinum, *J. Am. Chem. Soc.*, 1918, **40**, 1361–1402.

36 I. Langmuir, *"Part I" The Research Laboratory of the General Electric Company*, 1916, p. 2221.

37 I. Langmuir, *"Part II" The Research Laboratory of the General Electric Company*, 1918, p. 1848.

38 S. Hansen, An Adsorption Isotherm That Includes the Interactions Between Adsorbates, *J. Phys. Chem. C*, 2025, **129**, 5393–5407.

39 S. Arrhenius, Quantitative relationship between the rate a reaction proceed and its temperature, *J. Phys. Chem.*, 1889, **4**, 226–248.

40 A. Staykov, R. Komoda and M. Kubota, *et al.*, Coadsorption of CO and H_2 on an Iron Surface and Its Implication on the Hydrogen Embrittlement of Iron, *J. Phys. Chem. C*, 2019, **123**, 30265–30273.

41 A. Staykov, S. Fukumori and K. Yoshizawa, *et al.*, Interaction of SrO-terminated $SrTiO_3$ surface with oxygen, carbon dioxide, and water, *J. Mater. Chem. A*, 2018, **6**, 22662–22672.

42 G. Pekridis, K. Kalimeri and N. Kaklidis, *et al.*, Study of the reverse water gas shift (RWGS) reaction over Pt in a solid oxide fuel cell (SOFC) operating under open and closed-circuit conditions, *Catal. Today*, 2007, **127**, 337–346.

43 W. Tsai and W. H. Weinberg, Steady-State Decomposition of Ammonia on the Ru(001) Surface, *J. Phys. Chem.*, 1987, **91**, 5302–5307.

44 G. Ertl, Surface Science and Catalysis—Studies on the Mechanism of Ammonia Synthesis: The P. H. Emmett Award Address, *Chem. Rev.*, 1980, **21**, 201–223.

45 Z. Kowalczyk, J. Sentek, S. Jodzis, M. Muhler and O. Hinrichsen, Effect of Potassium on the Kinetics of Ammonia Synthesis and Decomposition over Fused Iron Catalyst at Atmospheric Pressure, *J. Catal.*, 1997, **167**, 407–414.

46 G. Centi and S. Perathoner, Adsorption and Reactivity of No on Copper-on-Alumina Catalysts: II. Adsorbed Species and Competitive Pathways in the Reaction of No with NH_3 and O_2, *J. Catal.*, 1995, **152**, 93–102.